

Dynamic Avalanches: Rate-Controlled Switching and Race Conditions

Lishuai Jin^{1,2,3} and Martin van Hecke^{1,2}

¹AMOLF, Science Park 104, 1098 XG Amsterdam, The Netherlands

²Huygens-Kamerlingh Onnes Lab, Universiteit Leiden, 2300 RA Leiden, The Netherlands

³Department of Mechanical Engineering, City University of Hong Kong, Hong Kong, China.

Avalanches are rapid cascades of rearrangements driven by cooperative flipping of hysteretic local elements. Here we show that flipping dynamics and race conditions—where multiple elements become unstable simultaneously—give rise to dynamic avalanches that cannot be captured by static models of interacting elements. We realize dynamic avalanches in metamaterials with controlled flipping times, and demonstrate how this allows to modify, promote, and direct avalanche behavior. Our work elucidates the crucial role of internal dynamics in complex materials and introduces dynamic design principles for materializing targeted pathways and sequential functionalities.

Quasistatic driving of multistable media, including crumpled sheets [1, 2], amorphous solids [3, 4], and metamaterials [5, 6], gives rise to dynamical orbits marked by sequences of rapid, irreversible transitions between metastable states. Under cyclic driving, these transitions form pathways which encode sequential shape morphing [7], memory effects [8–13], and computational capabilities of complex media [14–16]. Hence, key challenges include uncovering how the underlying physics shapes these pathways, identifying which pathways and combinations of pathways are physical, and realizing (meta)materials with tailored pathways for targeted functionalities [15–24].

Transitions often entail the flipping of bistable, hysteretic elements, such as ridges [5], particle clusters [25], beams [16], or hysteretic springs [26], which allows to distinguish two types of transitions. Transitions composed of a single flipping event are referred to as elementary, and those composed of multiple events are avalanches. These events occur in rapid succession, suggesting that avalanche characteristics may depend on the driving rate, the dynamics of individual flipping events, and the time delay between flipping events due to the finite velocity of signal propagation. For example, when the driving rate becomes comparable to the internal timescales, recent studies have shown that dynamic driving protocols can significantly influence the resulting avalanches [27–30].

Here, instead, we consider asymptotically slow driving and show that the internal dynamics can lead to *dynamic avalanches* that can not be described in a quasi-static framework. First, underdamped flipping dynamics can lead to vibrations and dynamical orbits that overshoot a local energy minimum, thus promoting the formation of avalanches. Second, when the time delay between flipping events is small, race conditions may occur where one flipping event destabilizes multiple other elements simultaneously [31–33]; the order in which these unstable elements flip then determines the avalanche.

We experimentally realize dynamic avalanches in metamaterials composed of hysteretic springs in which we control the flipping dynamics, and use simulations to reveal their underlying phase-space structure [16, 26]. We contrast our results to current models of interacting hys-

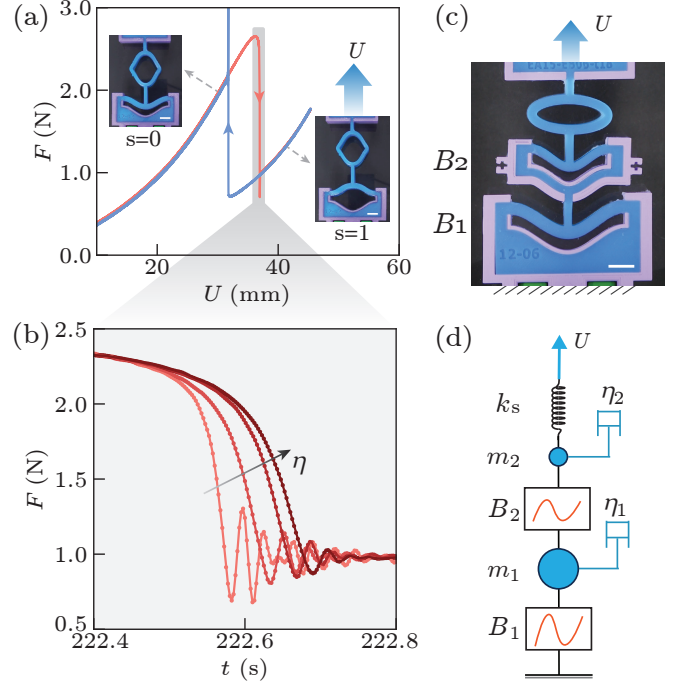


FIG. 1. (a) Force-extension response of a hysteretic element; insets show typical configurations for $s = 0$ and $s = 1$. (b) Zoom in of the $0 \rightarrow 1$ transition dynamics in air (light) and in silicon oils for viscosities $\eta = 350, 500, 1000$ cSt (increasingly dark). (c) Sample 1 is a metamaterial containing two hysteretic elements (B_1, B_2) coupled in series with an (elliptical) spring (scale bar 1 cm). (d) Numerical model of dynamic hysteretic elements, with spring constant k_s , masses m_1 and m_2 , and viscous dampers η_1 and η_2 .

terons [12–14]. Finally, we leverage our insights to design a metamaterial that exhibits six complex avalanches, enabling a challenging pathway that mimics a three-bit binary counter. Our work reveals the crucial role of internal timescales in slowly driven systems and paves the way for designer materials with novel pathways for advanced sensing and computation.

Multistable Metamaterials.— Networks of hysteretic springs [16, 26] are promising platforms to investigate and realize dynamic avalanches. We materialize hysteretic

springs using encased curved beams that flip between internal phase $s = 0$ (relaxed U-shape), and $s = 1$ (snapped shape) under tension (Fig. 1a) [16]. Experimentally, we control their flipping timescale through (partial) immersion in viscous fluids (Fig. 1b; see Appendix A). We focus on n hysteretic springs coupled in series for which the static properties, interactions, design and modeling are well understood (Fig. 1c) [16, 26], and in parallel perform simulations of a realistic model of dynamic hysteretic springs (Fig. 1d) [27, 28]. Under controlled deformation U , serial coupling leads to antiferromagnetic-like interactions, capable of producing avalanches [16, 26].

Dynamic Avalanches under Slow Driving.— We start by demonstrating that dynamic effects can promote avalanches. We represent the collective states of our metamaterial as $S = (s_1, s_2, \dots)$ and define the up and down switching thresholds at which element i becomes unstable when the control parameter U is increased or decreased as $U_i^\pm(S)$. We focus on a metamaterial made of two hysteretic springs and examine the transition triggered by destabilizing state (01) by lowering the driving U just below the switching threshold $U_2^-(10)$. In the simplest case, this results in an elementary transition (01) \rightarrow (00), which requires state (00) to be stable at $U = U_2^-(10)$ ¹, leading to the necessary condition:

$$G := U_1^-(10) - U_2^+(00) < 0, \quad (1)$$

where G is the gap between the relevant switching thresholds. However, when the flipping of the second element destabilizes the first element and cause it to flip upward from 0 to 1, the avalanche (01) \rightarrow (10) occurs. A sufficient condition for this avalanche is that $G > 0$, and in current hysteron models, this condition is taken as both sufficient and necessary [14, 32, 34–36].

To show that destabilization of the first element by the second can be promoted by dynamic effects, we design sample 1 with a small but negative value of G . We slowly sweep the global deformation U (rate 10 mm/min), measure all transitions and their associated switching thresholds, and collect these in a transition graph (t-graph) [9, 12–14, 37]. We first perform experiments when the sample is immersed in Polydimethylsiloxane oil (viscosity: 350 cSt) and then when the sample is suspended in air (Fig. 2; Appendix A). While the t-graph of the sample in oil is free of avalanches, the t-graph of the sample in air exhibits the avalanche (10) \rightarrow (01) despite $G < 0$ ² (Fig. 2). The observation of this avalanche and its dependence on the damping strongly points to the role of dynamic effects. Indeed, high-speed imaging of this avalanche reveals that the flipping dynamics of element one lead to an overshoot that triggers the switching of element two, just before element one reaches its '0' configuration (see Supplemental Material, Movie S1).

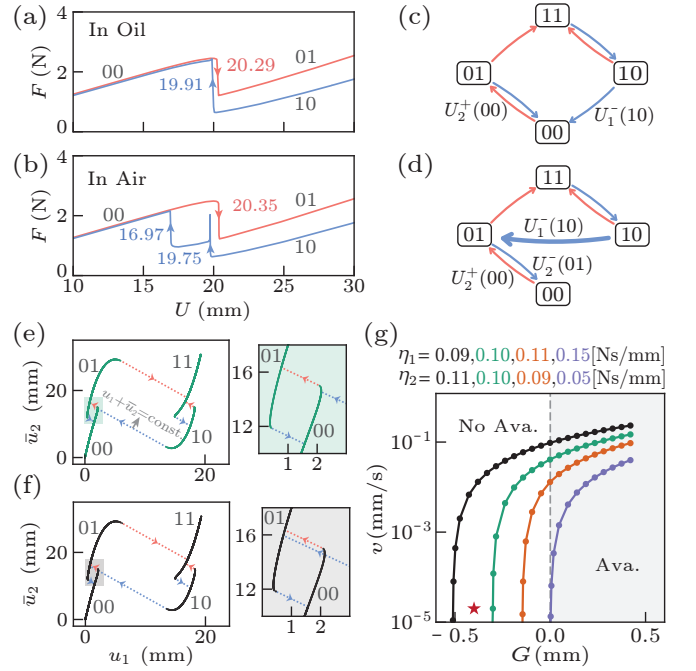


FIG. 2. (a,b) Force-extension curves for sample 1 submersed in oil (a) and air (b). The switching thresholds $U_2^+(00)$ and $U_1^-(10)$ for the up and down transitions of states (00) and (10) are indicated (as well as $U_2^-(01)$ in (b)). Both exhibit negative G . Note the overshoot of the force during the (10) \rightarrow (01) avalanche at $U = 19.75$ mm. (c,d) Corresponding t-graphs, with the associated switching thresholds indicated. (e,f) Orbits of the numerical model with $v := \dot{U} = 2 \cdot 10^{-5}$ mm/s, $G = -0.4$ mm, $m_i = (200, 100)$ g and $\eta_i = (0.10, 0.10)$ Ns/mm (e) and $\eta_i = (0.09, 0.11)$ Ns/mm (f), where $\bar{u}_2 = u_2 + u_k$, and $u_1 + \bar{u}_2 = U$. Zoom ins: In (e), dashed lines represent transitions (10) \rightarrow (00), (01) \rightarrow (00), and (00) \rightarrow (01); in (f), the transition (10) \rightarrow (00) is replaced by (10) \rightarrow (01). (g) Avalanche vs no-avalanche parameter regime for designs with the same masses, different pairs of η_i and range of G and v (star indicates G and v for panels (e,f)). Dynamic avalanches occur on the right side of each curve, including in regimes where the hysteron model predicts the absence of avalanches (white).

To further clarify how internal flipping dynamics can promote dynamic avalanches, even in the limit of quasistatic driving, we use a realistic numerical model which describes the evolution of the extensions u_i of hysteretic springs coupled to masses and viscous dampers (Fig. 1d; see Appendix B and Supplemental Material, Sec. II). The spring potentials control the switching thresholds and thus G , and the masses m_i and damping coefficients η_i control the internal dynamics [27, 28]. First, we fix the driving rate and masses, design the elements to feature a small negative gap G , and compare the trajectories $u_i(t)$ resulting from destabilizing state (10) by lowering U , for two different values of η_i (Fig. 2e,f). For $\eta_i = (0.10, 0.10)$, there is no avalanche and the trajectory lands on (00), where we note that since G has a numerical small value, the trajectory lands near the edge of instability of state

¹ We tacitly assume $U_2^+(00) < U_1^+(00)$.

² The values of the switching thresholds in air and in water are slightly different due to experimental errors.

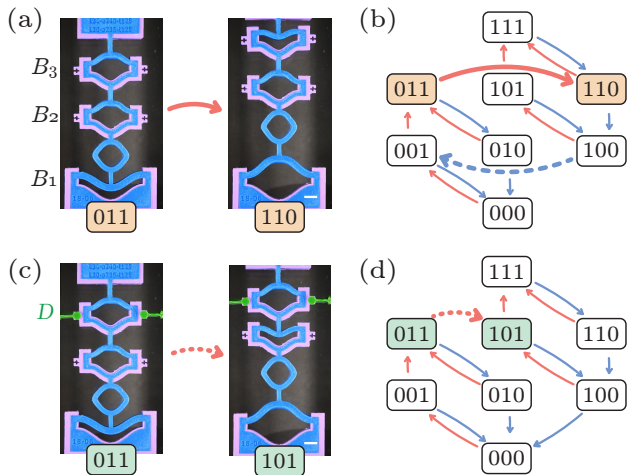


FIG. 3. **Race conditions.** Sample 2 features three serially coupled hysteretic elements ($B_1 - B_3$), a spring between B_1 and B_2 , and the third element can be damped (green). (a-b) Avalanche transition of sample 2 in air, and corresponding t-graph (for switching thresholds, see Supplemental Material, Fig. S9). The relevant gap for the $(011) \rightarrow (110)$ avalanche is positive, whereas the gap for $(100) \rightarrow (001)$ avalanche is negative, so that the latter is a dynamic avalanche which violates condition (i) i.e., the intermediate state 000 is stable (dashed). (c-d) Avalanche transition of sample 2, where element three is damped by submersing rigidly attached wings (D , green) in oil, and the corresponding t-graph. The $(011) \rightarrow (101)$ dynamics avalanche violates condition (ii) as it does not follow the scaffold (dotted). Scale bars, 1 cm.

(00) (Fig. 2e). In contrast, for $\eta_i = (0.09, 0.11)$ the orbit overshoots (00) and instead reaches state (01) (Fig. 2f). This illustrates how dynamic effects can lead to overshooting state (00), in particular when its range of attraction is small, thus triggering a dynamic avalanche (Supplemental Material, Movie S2).

We then study how the critical value of G , which separates the avalanche and no-avalanche regimes, depends on the driving rate v across a range of viscosity ratios η_i . Our data show that as $v \downarrow 0$, the critical value of G asymptotes to a constant, and that avalanches can occur for $G < 0$ over a wide range of viscosities (Fig. 2g). These avalanches are most strongly promoted when $\eta_1/\eta_2 \ll 1$, while for $\eta_1 \gg \eta_2$, the critical value of G approaches zero: in this regime, element two switches much faster than element one, allowing the system to quickly settle into the intermediate state. This shows that dynamical effects can promote, but not suppress avalanches, and that the internal flipping dynamics remains important even in the limit of quasistatic driving.

Race Conditions and Dynamic Steering.— We now consider race conditions, where one flipping event destabilizes multiple other elements simultaneously [31–33]³.

In random systems, the likelihood of race conditions increases with the number of elements [34]. In designed systems, such race conditions can be realized straightforwardly. The simplest race condition requires three elements, and we investigate the case where flipping element one of state (011) destabilizes both elements two and three. In particular we consider the case where both states (110) and (101) are stable at $U = U_1^+(011)$, so that dynamic effects, not only stability considerations, determine which state will be reached (for corresponding energy landscape, see Supplemental Material, Fig. S6). This race condition is materialized in sample 2 by making element one significantly larger than elements two and three: when, starting from state (011), element one snaps from 0 to 1, this significantly compresses and destabilizes both other elements. We verified this by selectively blocking either element two or three and observing that the other element became unstable (see Supplemental Material, Fig. S5).

Removing the blockades, we show that the resulting avalanche can be selected by viscous damping. In air, the sample 2 exhibits the $(011) \rightarrow (110)$ avalanche (Fig. 3a-b), whereas when the third element is submersed in oil, sample 2 exhibits the $(011) \rightarrow (101)$ avalanche transition (Fig. 3c-d). High-speed imaging shows that the flipping of element one leads to compression of element two and then three, where the delay originates from the finite propagation speed of the perturbation induced by the first snap. In air, even though element two is transiently compressed, eventually element three flips, thus releasing the pressure on element two, whereas in oil, the damping of element three slows down its evolution and forces element two to flip (Supplemental Material, Movie S3). Numerical simulations of this race condition scenario are consistent with the experimental observations, and moreover show that by only moving the location of springs and masses, we can further tune the resulting transitions, stressing the importance of the propagation of information through the sample (Supplemental Material, Fig. S7). Together, this shows that race conditions allow dynamic effects to qualitatively steer avalanche pathways; and as we discuss below, allow to realize t-graphs that are inconsistent with all current hysteron models (Fig. 3d).

Quasistatic and Sequential Models.— We now compare the observed avalanches to those of current hysteron models, which model the elements as strictly binary elements [13, 14, 32]. Their interactions are encoded via the state dependence of the switching thresholds $U_i^\pm(S)$, which sometimes can be modeled theoretically [12, 13, 38]. In the absence of internal dynamical rules, the switching thresholds fully determine the transitions and avalanches. For race conditions, which become prevalent in large systems [34], the model is sometimes deemed ill-defined [14] or a phenomenological rule—like flip the most unstable hysteron—is employed [13, 34].

³ Race conditions are distinct from degeneracies that occur when

multiple switching thresholds are equal.

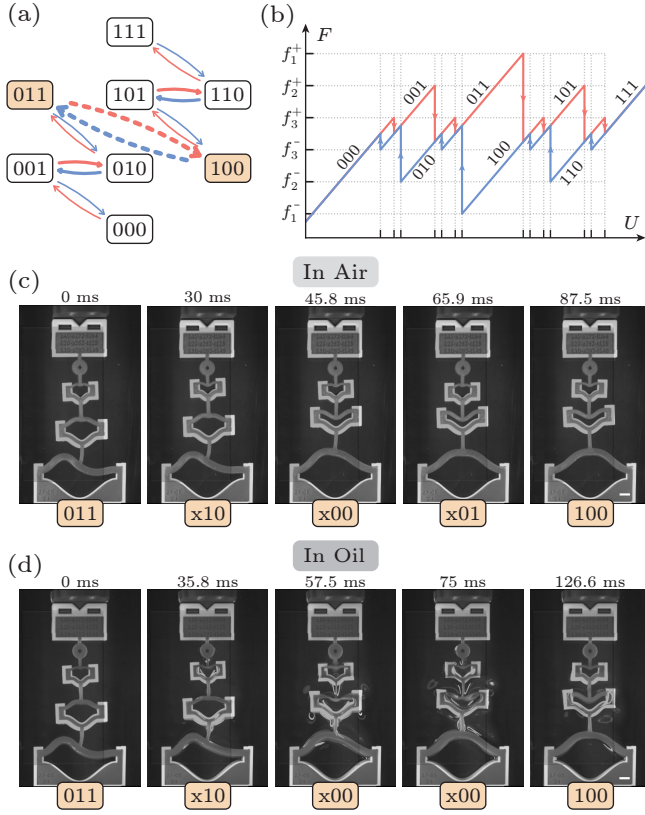


FIG. 4. **Three-bit counter.** (a) T-graph of a three-bit counter. (b) Target curve $F(U)$. (c,d) High-speed images during the avalanche transition in air and in silicone oil. Scale bars, 1 cm.

Avalanches then proceed by sequential flipping of hysterons, thus visiting intermediate states that are separated by one flipping event. This sequential assumption has two consequences. (i) Avalanches only proceed when these intermediate states are unstable, such that condition $G > 0$ is both necessary and sufficient. (ii) Avalanches and transitions follow the same scaffold [32]; in other words, if the system exhibits the elementary transition $S_1 \rightarrow S_2$, then an avalanche where S_1 is an intermediate state also evolves to S_2 .

Clearly, sample 1 and sample 2 in air violate condition (i), while the partially damped sample 2 violates condition (ii) (Fig. 3d). To see this, note that the up avalanche starting from (011) has the intermediate state (111), which itself has an elementary transition to (110). Hence, the avalanche (011) \rightarrow (110) is consistent with the scaffold (Fig. 3b), but the avalanche (011) \rightarrow (101) displayed by the partially immersed sample 2 is not (Fig. 3d). Hence, qualitative and quantitative features of dynamic avalanches are inconsistent with sequential, quasistatic models.

Three-bit counter.— We next harness race conditions and dynamic effects to create a metamaterial which exhibits a challenging pathway that is inspired by a three-bit counter, i.e. evolves as (000) \leftrightarrow (001) \leftrightarrow (010) \leftrightarrow

$\dots \leftrightarrow$ (111), which requires six avalanches (Fig. 4a). Crucially, the pair of avalanches (011) \leftrightarrow (100) require race conditions; as shown previously, sequential avalanches for serially coupled hysteretic elements are restricted to those where two elements change phase in the opposite direction [16]. To realize this pathway, we define a target curve for the collective force-displacement $F(U)$ (Fig. 4b), and consider the design problem of serially coupled bilinear elements each described as $f_i = k_i u_i - g_i s_i$, where g_i are the force jumps resulting from the switching of the i -th hysteron (Appendix, Fig. A1b) [16, 26]. This target curve can be realized with three serially coupled elements with hierarchically organized ‘sizes’, i.e., where the switching thresholds satisfy $f_1^- < f_2^- < f_3^- < f_3^+ < f_2^+ < f_1^+$, where $g_1 > g_2 > g_3$, and where race conditions allow the challenging avalanches (011) \leftrightarrow (100) (see Appendix C).

We realize sample 3 based on such considerations, using three elements of increasing size (Fig. 4c-d). Its $F(U)$ curve satisfies the design target, including the nested ordering of the switching forces $F^\pm(S)$ and the correct sequential ordering of all switching thresholds $U^\pm(S)$. Although the detailed evolution of the sample during the anomalous avalanche (011) \leftrightarrow (100) depends on whether the sample is in air or in oil, in both cases, the elements switch simultaneously thus evidencing the race condition. This demonstrates that race conditions can be leveraged to realize (meta)materials with challenging pathways (Fig. 4a and Supplemental Material, Movie S4).

Discussion and Outlook.— Although the underlying static energy landscape determines the states, their stability, and the initial mode of evolution after an instability, the physical dynamics is crucial to fully capture the irreversible transitions between states [27, 28]. In general, there are three overall time scales at play - the inverse global strain rate $\dot{\gamma}^{-1}$, the typical time for a transition wave to cross one element τ^w , and the switching times of the elements τ_i^s , where in particular the latter can vary with each element. When $\dot{\gamma}^{-1} \gg \tau^w L \gg \tau_i^s$, where L is the linear size in number of elements, and when the dynamics is overdamped, all time scales are separated, race conditions are irrelevant, and flipping events occur in isolation with each event forming a smooth connection between intermediate states — although we note that even in this limit, the sequence of flipping may be determined by the spatial separation between elements, something that is missing in current hysteron models. But when the condition $\tau^w L \gg \tau_i^s$ is no longer satisfied, or when the flipping events are underdamped, the trajectories between states are intrinsically dynamical, with controlled flipping dynamics and race conditions allowing to materialize avalanches that quantitatively and qualitatively deviate from sequential hysteron models. Our dynamic design strategy imbues metamaterials with unprecedented sensing capabilities, where avalanches depend on ambient viscosities (Fig. 2), or where more complex situations, such as race conditions, could be tuned to compare different viscosities in materia (Fig. 3). More-

over, at fixed damping, our dynamic strategy allows controlled avalanches for accelerated shape-morphing [39], autonomous soft robots [18], and designer pathways (that are inconsistent with current hysteron models), thus aiding the design of metamaterials with emergent memory and computing [7, 16, 40].

Acknowledgments

We thank D. Shohat, P. Baconnier, J. Liu, and M. Liu for insightful discussions, and D. Ursem for technical support. L. J. and M. v. H. acknowledge funding from European Research Council Grant ERC-101019474.

-
- [1] K. Matan, R. B. Williams, T. A. Witten, and S. R. Nagel, Crumpling a thin sheet, *Physical Review Letters* **88**, 076101 (2002).
 - [2] D. Shohat, D. Hexner, and Y. Lahini, Memory from coupled instabilities in unfolded crumpled sheets, *Proceedings of the National Academy of Sciences* **119**, e2200028119 (2022).
 - [3] C. Reichhardt, I. Regev, K. Dahmen, S. Okuma, and C. Reichhardt, Reversible to irreversible transitions in periodic driven many-body systems and future directions for classical and quantum systems, *Physical Review Research* **5**, 021001 (2023).
 - [4] D. Fiocco, G. Foffi, and S. Sastry, Encoding of memory in sheared amorphous solids, *Physical Review Letters* **112**, 025702 (2014).
 - [5] A. Meeussen and M. van Hecke, Multistable sheets with rewritable patterns for switchable shape-morphing, *Nature* **621**, 516 (2023).
 - [6] J. T. Overvelde, T. Kloek, J. J. D'haen, and K. Bertoldi, Amplifying the response of soft actuators by harnessing snap-through instabilities, *Proceedings of the National Academy of Sciences* **112**, 10863 (2015).
 - [7] D. Melancon, A. E. Forte, L. M. Kamp, B. Gorissen, and K. Bertoldi, Inflatable origami: Multimodal deformation via multistability, *Advanced Functional Materials* **32**, 2201891 (2022).
 - [8] J. D. Paulsen and N. C. Keim, Mechanical memories in solids, from disorder to design, *Annual Review of Condensed Matter Physics* **16** (2024).
 - [9] J. D. Paulsen and N. C. Keim, Minimal descriptions of cyclic memories, *Proceedings of the Royal Society A* **475**, 20180874 (2019).
 - [10] N. C. Keim and S. R. Nagel, Generic transient memory formation in disordered systems with noise, *Physical Review Letters* **107**, 010603 (2011).
 - [11] J. D. Paulsen, N. C. Keim, and S. R. Nagel, Multiple transient memories in experiments on sheared non-brownian suspensions, *Physical Review Letters* **113**, 068301 (2014).
 - [12] C. W. Lindeman and S. R. Nagel, Multiple memory formation in glassy landscapes, *Science Advances* **7**, eabg7133 (2021).
 - [13] N. C. Keim and J. D. Paulsen, Multiperiodic orbits from interacting soft spots in cyclically sheared amorphous solids, *Science Advances* **7**, eabg7685 (2021).
 - [14] M. van Hecke, Profusion of transition pathways for interacting hysterons, *Physical Review E* **104**, 054608 (2021).
 - [15] L. J. Kwakernaak and M. van Hecke, Counting and sequential information processing in mechanical metamaterials, *arXiv preprint arXiv:2302.06947* (2023).
 - [16] J. Liu, M. Teunisse, G. Korovin, I. R. Vermaire, L. Jin, H. Bense, and M. van Hecke, Controlled pathways and sequential information processing in serially coupled mechanical hysterons, *Proceedings of the National Academy of Sciences* **121**, e2308414121 (2024).
 - [17] J. Ding and M. van Hecke, Sequential snapping and pathways in a mechanical metamaterial, *The Journal of Chemical Physics* **156** (2022).
 - [18] L. M. Kamp, M. Zanaty, A. Zareei, B. Gorissen, R. J. Wood, and K. Bertoldi, Reprogrammable sequencing for physically intelligent under-actuated robots, *arXiv preprint arXiv:2409.03737* (2024).
 - [19] T. Jules, A. Reid, K. E. Daniels, M. Mungan, and F. Lechenault, Delicate memory structure of origami switches, *Physical Review Research* **4**, 013128 (2022).
 - [20] H. Bense and M. van Hecke, Complex pathways and memory in compressed corrugated sheets, *Proceedings of the National Academy of Sciences* **118**, e2111436118 (2021).
 - [21] L. Jin, C. Meulblok, M. van Hecke, *et al.*, Multiperiodic responses and memory effects in frustrated sheets, *Bulletin of the American Physical Society* (2024).
 - [22] A. El Elmi and D. Pasini, Tunable sequential pathways through spatial partitioning and frustration tuning in soft metamaterials, *Soft Matter* **20**, 1186 (2024).
 - [23] C. Sirote-Katz, D. Shohat, C. Merrigan, Y. Lahini, C. Nisoli, and Y. Shokef, Emergent disorder and mechanical memory in periodic metamaterials, *Nature Communications* **15**, 4008 (2024).
 - [24] L. P. Hyatt and R. L. Harne, Programming metastable transition sequences in digital mechanical materials, *Extreme Mechanics Letters* **59**, 101975 (2023).
 - [25] J. Wang, J. Schwarz, and J. D. Paulsen, Propagating irreversibility fronts in cyclically sheared suspensions, *Physical Review Research* **4**, 013025 (2022).
 - [26] D. Shohat and M. van Hecke, Geometric control and memory in networks of hysteretic elements, *Physical Review Letters* **134**, 188201 (2025).
 - [27] C. W. Lindeman, V. F. Haghighi, C. I. Ip, and S. R. Nagel, Competition between energy and dynamics in memory formation, *Physical Review Letters* **130**, 197201 (2023).
 - [28] T. Jules, L. Michel, A. Douin, and F. Lechenault, When the dynamical writing of coupled memories with reinforcement learning meets physical bounds, *Communications Physics* **6**, 25 (2023).
 - [29] M. Liu, M. Gomez, and D. Vella, Delayed bifurcation in elastic snap-through instabilities, *Journal of the Mechanics and Physics of Solids* **151**, 104386 (2021).
 - [30] W. Huang, T. Yu, D. Vella, K. J. Hsia, and M. Liu, Exploiting dynamic bifurcation in elastic ribbons for mode skipping and selection, *Journal of the Mechanics and Physics of Solids* **190**, 105721 (2024).
 - [31] D. A. Huffman, The synthesis of sequential switching circuits, *Journal of the Franklin Institute* **257**, 161 (1954).
 - [32] M. H. Teunisse and M. van Hecke, Transition graphs of interacting hysterons: Structure, design, organization

- and statistics, arXiv preprint arXiv:2404.11344 (2024).
- [33] A. Szulc, M. Mungan, and I. Regev, Cooperative effects driving the multi-periodic dynamics of cyclically sheared amorphous solids, *The Journal of Chemical Physics* **156** (2022).
 - [34] P. Baconnier, M. H. Teunisse, and M. van Hecke, Proliferation and prevention of self-loops in ensembles of interacting binary elements, arXiv preprint arXiv:2412.12658 (2024).
 - [35] M. Mungan, S. Sastry, K. Dahmen, and I. Regev, Networks and hierarchies: How amorphous materials learn to remember, *Physical Review Letters* **123**, 178002 (2019).
 - [36] M. Mungan and M. M. Terzi, The structure of state transition graphs in systems with return point memory: I. general theory, in *Annales Henri Poincaré*, Vol. 20 (Springer, 2019) pp. 2819–2872.
 - [37] I. Regev, I. Attia, K. Dahmen, S. Sastry, and M. Mungan, Topology of the energy landscape of sheared amorphous solids and the irreversibility transition, *Physical Review E* **103**, 062614 (2021).
 - [38] C. W. Lindeman, T. R. Jalowiec, and N. C. Keim, Generalizing multiple memories from a single drive: The hysteron latch, *Science Advances* **11**, eadr5933 (2025).
 - [39] L. Jin, R. Khajehtourian, J. Mueller, A. Rafsanjani, V. Tournat, K. Bertoldi, and D. M. Kochmann, Guided transition waves in multistable mechanical metamaterials, *Proceedings of the National Academy of Sciences* **117**, 2319 (2020).
 - [40] J. D. Paulsen, Mechanical hysterons with tunable interactions of general sign, arXiv preprint arXiv:2409.07726 (2024).

Appendix

A. Experimental Methods and Samples

We realize multistable metamaterials by coupling n bistable, hysteretic springs in series with an elliptical-shaped, nearly-linear spring, which facilitate sharp snapping transitions [16]. Each hysteretic spring consists of a pre-curved flexible beam encapsulated within a rigid 3D-printed clamp. The flexible beams of the samples are fabricated from a two-component siloxane rubber (Mold Star 30, Smooth On) using standard molding techniques, while the rigid components consist of 3D-printed polylactic acid (PLA) frames produced with an Ultimaker S3 printer.

Isolated elements switch up ($s_i : 0 \rightarrow 1$) when their extension u_i exceeds the bare switching threshold u_i^+ , and switch down ($s_i : 1 \rightarrow 0$) when u_i falls below u_i^- . The beams' thickness t_i , span L_i and the amplitude of the beam's profile A_i determine these switching thresholds. For detailed design parameters for each of our samples, see Supplemental Material.

The mechanical response of our samples is characterized using a horizontal tensile testing machine (Instron 5965), which provides precise control over axial displacement U with an accuracy better than $4 \mu\text{m}$. A 100 N load cell is employed to measure the applied force with a res-

olution down to 0.5 mN. All experiments are conducted at a constant displacement rate of 10 mm/min. During testing, the samples are imaged using both a Canon camera (EOS 800D) and a high-speed camera (Phantom v4.2) to capture their dynamic evolution. The samples are tested either in air or fully or partially immersed in Polydimethylsiloxane oil (viscosity: 350 cSt) for various damping conditions. To implement partial submersion of a hysteron, we mount two wings (green parts in Fig. 3c) to its sides. The wings are then immersed in silicone oil while the rest of the sample remains clear of the oil, creating a partially damped environment for the sample.

B. Numerical Model

To investigate the dynamical behavior of coupled bistable elements, we perform simulations of a simple mechanical model introduced recently [27, 28]. This model represents networks of bistable springs, linear springs, masses and viscous dampers (Fig. 1d). First, each bistable spring is represented with a cubic force-displacement curve $f_i(u_i)$. Second, the elliptical spring in our samples is represented by a linear spring $f_k(u_k)$. The detailed forms of $f_i(u_i)$ and $f_k(u_k)$ can be obtained from fitting to finite element simulations of our samples, or can be adjusted to represent the range of stability of the states [16, 26–28]. Together, networks of these elements describe the stable and unstable collective states and exhibit hysteretic transitions between stable states.

To model how the transition pathways depend on dynamical effects, the model is augmented with masses and viscous dampers. For example, sample 1, consisting of two hysteretic elements coupled to an elliptical ring, is modeled as follows:

$$\begin{aligned} m_1 \ddot{x}_1 + \eta_1 \dot{x}_1 + f_1(u_1) - f_2(u_2) &= 0, \\ m_2 \ddot{x}_2 + \eta_2 \dot{x}_2 + f_2(u_2) - f_k(u_k) &= 0, \\ u_1 + u_2 + u_k &= U, \end{aligned} \quad (\text{B1})$$

where m_i represents the masses that are coupled to viscous dampers characterized by η_i (Fig. 1d). For details, see Supplemental Material.

C. Design of Three-Bit Counter

We consider the design of a targeted pathway that materializes a three-bit binary counter (Fig. A1a). We start from a simple model of three serially coupled bilinear elements, each describe by [16, 26]:

$$f_i = k_i u_i - g_i s_i. \quad (\text{C1})$$

Here f_i and u_i are the forces and extensions, k_i is the stiffness, and g_i is the force jump between $s_i = 0$ and $s_i = 1$ branches; each element switches between these branches when u_i exceeds the switching thresholds u_i^\pm ,

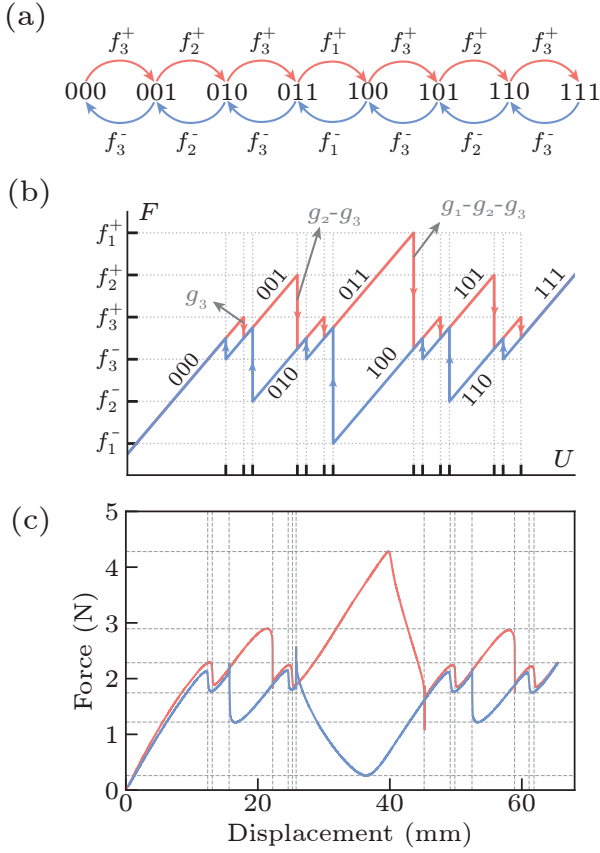


FIG. A1. **Design of three-bit counter.** (a) The transitions between subsequent states must occur at one of the six critical switching forces. (b) Target curve $F(U)$. (c) Experimentally observed $F(U)$ curve for sample 3, with critical forces and displacements highlighted.

or equivalently, when the force exceeds the critical forces f_i^\pm . Mechanical balance equations dictate that the global force $F = f_1 = f_2 = f_3$, and that the global extension $U = u_1 + u_2 + u_3$, which, under controlled extension U , allows to construct the $F(U)$ curve [16, 26].

The target $F(U)$ curve is constructed such that,

for each value of U , at most two stable states exist (Fig. A1b). This ensures unambiguous transitions that do not rely on the dynamic effects of type (i) to be controlled. Moreover, the target pathway specifies the sequence of flipping events, and as each flipping event is associated with a specific critical force f_i^\pm , this implies that these have to be nested as in Fig. A1b, i.e.

$$f_1^- < f_2^- < f_3^- < f_3^+ < f_2^+ < f_1^+ . \quad (C2)$$

Similarly, the 14 critical values of U satisfy a chain of inequalities of the form $U_3^-(001) < U_3^+(000) < \dots < U_3^-(111) < U_3^+(110)$, and translating these to the switching forces and force drops, and using elementary algebra, yields a second set of design equations (where we assume $k_i = 1$ without loss of generality)

$$\begin{aligned} & f_3^- + g_3 < f_3^+ < f_2^- + g_2 < f_2^+ + g_3 \quad \dots \\ \dots & < f_3^- + g_2 + g_3 < f_3^+ + g_2 < f_1^- + g_1 \quad \dots \\ \dots & < f_1^+ + g_2 + g_3 < f_3^- + g_1 + g_3 < f_3^+ + g_1 \quad \dots \\ \dots & < f_2^- + g_1 + g_2 < f_2^+ + g_1 + g_3 \quad \dots \\ \dots & < f_3^- + g_1 + g_2 + g_3 < f_3^+ + g_1 + g_2 . \end{aligned} \quad (C3)$$

There is a range of choices for the switching forces and force drops g_i —which both can be designed experimentally at the level of individual elements—that satisfy these equations. For example, an equidistant ordering of the switching fields requires rapidly growing values of the force drop g_i with significance of the elements. Hence, in our experimental design we take each element to satisfy the nested constraints on the critical forces, and the rapidly increasing values of the force drops. After some iterative design, this produced sample 3, which satisfies both sets of design equations (Fig. A1c). Note that while sample 3 exhibits sharp transitions between states in the correct order, the deformation of the largest element exhibits higher beam modes, which modify $f_1(u_1)$ and make the collective curve $F(U)$ deviate from the strictly piecewise linear target - we stress that the sequence of transitions is correct. This deviation shows the robustness of our design strategy to such experimental deviations.